Microstructure and magnetic properties of as-cast Ni_2MnGa rods and tubes solidified by suction casting

G. Pozo-López [a,b,*], A. M. Condó [c], S. P. Limandri [a,b], R. H. Mutal [a,b], E. Winkler [c], S. E. Urreta [a], L. M. Fabietti [a,b]

[a] *Universidad Nacional de Córdoba, FAMAF, Córdoba, Argentina.*

[b] *CONICET, IFEG, Córdoba, Argentina.*

[c] *Centro Atómico Bariloche (CNEA, CONICET), Instituto Balseiro (UNCuyo, CNEA), S.C. de Bariloche, Río Negro, Argentina.*

[*]Author to whom correspondence should be addressed: Gabriela Pozo-López: gabriela.pozo.lopez@unc.edu.ar. Facultad de Matemática, Astronomía, Física y Computación, Universidad Nacional de Córdoba, Ciudad Universitaria, X5000HUA, Córdoba, Argentina.

Abstract

Ni_2MnGa cylinders and tubes are solidified in water chilled copper molds, a few millimeters in external diameter and five centimeters long, by the suction casting technique. At room temperature, all samples are in cubic austenitic phase. Microstructure and crystallographic texture of the as-cast rods and tubes are characterized by XRD, SEM, EBSD and TEM. Because of the heat extraction geometry samples exhibit a strong texture, with the [100] direction preferentially oriented in the radial direction, together with a random distribution on the long axis. This texture is more marked in the tubes. XRD and TEM results indicate that the major austenitic phase is *fcc*, with $L2_1$ order. A minority volume of the equilibrium B2´ disordered phase is detected by the presence of two close Curie temperatures in cylinders and tubes 2 mm in external diameter, but not when this diameter is near 1 mm. Precipitates of the stable compounds α-Mn(S,Se), with a NaCl-type structure, and monoclinic P_4S_5 are observed in all the samples. Cylinders and tubes in austenitic phase are magnetically soft. Hysteresis loops in martensitic phase exhibit local steps associated to a magnetization mechanism involving twin boundary displacement, indicating that a field-induced variant reordering takes place. The switching field H_{sw}, corresponding to the magnetization step observed, is identified as the field at which twin boundaries become mobile. The measured values of 0.37 T to 0.49 T are consistent with those corresponding to the onset of Type I twin boundaries displacement in 5M martensite, with an equivalent threshold stress of 1 MP.

Keywords: Ni_2MnGa; Ferromagnetic shape–memory alloys; Suction casting; Microstructure; Martensitic transformation; Magnetic properties.

1. Introduction

Ferromagnetic shape memory (FSM) alloys are a new class of smart and multifunctional materials that combine the properties of ferromagnetism with those of the thermoelastic martensitic transformation. In these alloys, recoverable strains of up to 10% can be induced by magnetic fields, which is an order of magnitude higher than the maximum induced strains found in piezoelectric and magnetostrictive materials, usually used in actuation and control systems [1]. These magnetic-field-induced strains (MFIS) are a consequence of the motion of twin boundaries induced by the magnetic field, in the ferromagnetic martensitic phase of the system, which presents a high magnetocrystalline anisotropy [2]. The large MFIS, together with the rapid response to the magnetic field (in comparison with the thermal response), makes this magneto-mechanical phenomenon very interesting, in view of its practical application in magnetic sensors or actuators, able to work at high frequencies and without variation of the external temperature.

In the last decades, Ni-Mn-Ga alloys with chemical compositions close to the stoichiometric compound Ni_2MnGa have become the most attractive ones in the family of ferromagnetic shape memory materials. They undergo a thermoelastic martensitic transformation from a cubic austenitic phase, with $L2_1$ Heusler-type structure, to a lower-symmetry martensitic phase on cooling from high temperature [3,4]. Depending on chemical composition, thermal history and stress state, different kinds of martensite can be observed: five-layered (5M) [5,6] or seven-layered (7M) [6,7] modulated monoclinic martensitic structure, or a nonmodulated (NM) tetragonal martensite structure [6,8]. Moreover, the microstructure, properties and martensitic transformation temperatures of these alloys can further be tuned by the whole preparation route [9]. Since the martensitic transition temperature T_M is lower than the Curie point T_C for these alloys (T_M = 202 K and T_C = 376 K for the stoichiometric composition [3]) martensitic transformation occurs between two ferromagnetic phases. Ullakko *et al.* [2] are credited with first suggesting the possibility of a magnetic field-controlled shape memory effect in these materials. In 1996, they reported a magnetic-field-induced strain of nearly 0.2% under a magnetic field of 0.8 T in Ni_2MnGa single crystals. Lately, magnetic-field-induced strains of

approximately 6% and 10 % were reported for off-stoichiometric Ni-Mn-Ga single crystals of 5M [5,10] and 7M [7] martensitic phases, respectively. In addition to exhibiting the greatest MFIS, Ni-Mn-Ga alloys also present other multifunctional properties such as superelasticity [11], giant magnetocaloric effect [12] and negative magnetoresistance [13].

Magnetic-field-induced strains in polycrystalline Ni-Mn-Ga alloys are vanishingly small compared to the ones obtained for single crystals, because the random distribution of crystallographic orientations greatly weakens the field controlled functional behavior [14,15]. However, from the application point of view, research has been directed towards polycrystalline materials because of their much simpler and lower-cost fabrication process. Larger MFIS can be generated in magnetically trained, highly textured, coarse-grained or highly porous samples, in the form of thin films, ribbons, textured polycrystalline bulks or foams [15-19]. In this sense, ultra-rapid solidification routes, such as single- and double-roller melt-spinning techniques, have been successfully adopted as effective single-step processes to produce nearly homogeneous Ni_2MnGa ribbons, in which the crystallographic texture and the internal stress state in the material give rise to the magnetic shape memory effect [20-23]. Another rapid solidification technique achieving lower quenching rates (~10^2 K/s) is the suction casting method [24,25], which allows the production of bulk samples with different crystallographic textures and internal stresses. In this process, an arc-melted alloy is sucked into a water-cooled copper mold by a sudden pressure difference between the mold and the main chamber [26]. Very few data are available concerning the shape memory effect in polycrystalline Ni-Mn-Ga as-cast cylinders, solidified by this method.

The aim of the present work is to obtain, by the suction casting technique, bulk polycrystalline cylinders/tubes of the extremely brittle Ni_2MnGa phase exhibiting magnetic-field-induced strain. A detailed study of the microstructure, crystallographic texture, structural and magnetic transformation temperatures and magnetic properties of the as-cast samples indicates that the magnetization mechanism in the martensitic phase involves magnetic field-induced rearrangement (MIR) of martensitic variants via twin boundary motion, which is at the origin of field-induced strain. Resulting samples have macroscopic dimensions, of the order of

millimeters in diameter and about 4 cm in length, so they can be used in actuators of small and medium size, with relatively good mechanical strength.

2. Materials and methods

A master alloy of nominal composition Ni_2MnGa was prepared by arc melting 99.9% pure Ni (Strem Chemicals), 99.95% pure Mn (Alfa Aesar) and 99.99% pure Ga (Strem Chemicals). The small ingots so obtained (about 5 g) were re-melted four times to promote a homogeneous distribution of the components. All these procedures were conducted under a Zr gettered Ar atmosphere, with a weight loss during arc melting less than 0.4%.

The arc furnace used in this study can work in melting or suction casting modes. In the latter one, a special water-cooled suction casting unit is adjusted to the copper base with a hole in the central part, enabling the formation of rods or tubes by suctioning the molten alloy into cylindrical copper molds 1-3 mm diameter and 50 mm length (see Figure 1). Varying the mass of the molten alloy (small pieces cut from the master ingots) and removing the base of the cylindrical copper molds, solid cylinders or thin walled tubes can be produced.

Samples in the form of rods (cylinders) of 1 and 2 mm diameter (named C1 and C2, respectively) and tubes of 2 mm outer diameter (T2) were produced, as shown in Figure 2. Mean outer diameter *D*, length *l* and wall thickness *w* of the samples are summarized in Table 1.

Table 1

Mean outer diameter *D*, length *l* and wall thickness *w* of the cylinders and tubes produced by the suction casting technique.

Sample	C1	C2	T2
D [mm]	1.17 ± 0.04	1.96 ± 0.04	1.91 ± 0.02
l [mm]	44 ± 2	41 ± 2	30 ± 3

w [μm]	200 ± 60

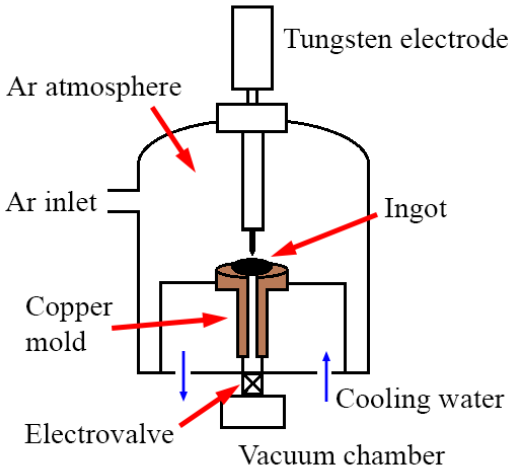

Figure 1. Schematic diagram of the suction casting furnace.

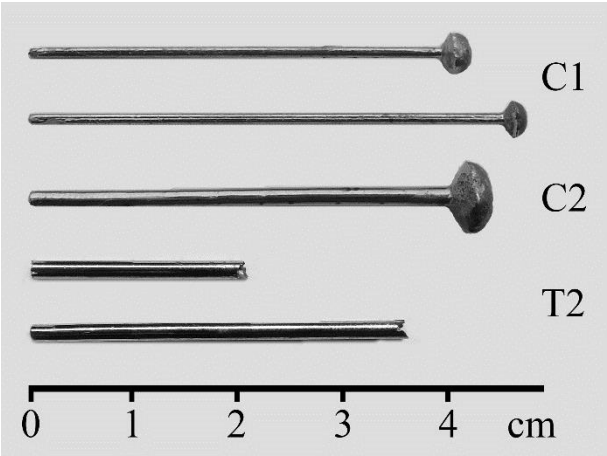

Figure 2. Typical suction-cast rods (C1 and C2) and tubes (T2).

The resulting microstructures were characterized by X-ray diffraction (XRD), confocal microscopy (CLSM), scanning electron microscopy (SEM) and transmission electron microscopy (TEM). Room temperature X-ray diffraction profiles were recorded in a PANalytical Empyrean diffractometer, in the 2θ range from 10º to 100º, using Cu Kα radiation

(λ= 1.5418 Å). An Olympus LEXT OLS4000 confocal microscope was used to image the rods and tubes fracture surfaces.

Texture studies were performed by means of the electron backscattered diffraction technique (EBSD) in a FE-SEM Σigma (Carl Zeiss) scanning electron microscope, equipped with an Oxford Nordlys Nano electron backscatter detector, with a CCD camera of 1344×1024 pixels and a 40 mm × 35 mm front phosphor screen. EBSD maps were collected with a 20 keV incident energy, 60 and 120 μm apertures, 70° sample tilt and a working distance of 8.5 mm. Samples for EBSD observations were included in aluminum (to enhance conductivity) and mechanically polished with 600, 1000 and 2000 grit polishing papers, 6 mm, 3 mm and 1 mm diamond pastes, and colloidal silica (0.05 μm). Final chemomechanically polish was carried out in a VibroMet™ 2 Vibratory Polisher using a MasterMet™ colloidal silica suspension (Buehler). The AZtec 3.1 software (Oxford Instruments) was employed for phase indexing and deconvolution. Crystallographic data given by ICSD card #103803 (Ni_2MnGa, space group *F m -3 m*) was considered to identify the crystal orientations in EBSD patterns. A 4×4 binning was used for the CCD camera while 10 bands and 80 Hough transform quality were considered for pattern indexation. Maps were acquired with steps ranging from 1 μm to 3 μm depending on the sample. These steps were chosen to optimize the measurement time and to ensure at least five points per grain. EBSD maps and pole figures were processed using the Tango and Mambo modules in the Oxford Instruments/HKL Channel 5 software package.

Transmission electron microscopy (TEM) observations and selected area diffraction patterns were performed in a Philips CM200 UT and a FEI TECNAI F20 G2 microscopes, operating at 200 kV and equipped with energy-dispersive X-ray spectroscopy (XEDS) facility. To prepare the samples for TEM observation, slices about 0.5 mm thick, were spark-cut from the rods; in the case of the tubes, small pieces (< 3 mm long) were obtained fracturing the brittle walls. Tripod polishing was used as a preliminary step for the final twin-jet electropolishing. The slices and bits were thin down to obtain flat, ~100 μm thick, samples. The resulting foils were then twin-jet electropolished with a 20% HNO_3 (nitric acid) / 80% pro-analysis methanol electrolyte, at 12 V and 258 K.

Magnetization as a function of temperature curves $\sigma(T)$ were measured in a Quantum Design SQUID magnetometer, in the temperature range 5-300 K, under an applied field of 2 mT. Magnetization isotherms $\sigma(H)$ curves were recorded at selected temperatures within that range, up to a maximum field of 1.5 T. Samples for magnetic measurements were thin slices cut from the rods and small broken pieces of the tubes walls, in a way that demagnetizing factors could be neglected. Curie temperatures were estimated from magnetization vs. temperature curves measured in a Faraday balance, in the 290 K - 400 K temperature range.

3. Results and Discussion

3.1 X-ray diffraction analysis

Room temperature XRD patterns of the external surfaces of the as-cast rods and tubes are shown in Figure 3. Diffractograms were indexed according to an ordered $L2_1$ crystal structure since, in addition to the fundamental diffraction lines [$(h+k+l)/2=2n$], even [$(h+k+l)/2=2n+1$] and odd [h, k, and l = odd numbers] superlattice reflections were clearly identified [3,27]. Secondary phases were not detected.

The lattice parameter a of the $L2_1$ austenitic phase in each sample was calculated from the angular positions of the fundamental reflections 220, 400, 422 and 440 after a profile fitting with Pearson VII functions, and correcting the 2θ values so obtained by considering the zero shift effect as described in [28]. The resulting values, listed in Table 2, are indistinguishable within experimental errors and quite similar to the value a_0 = 5.825 Å reported by Webster *et al.* [3] and tabulated in card ICSD #103803.

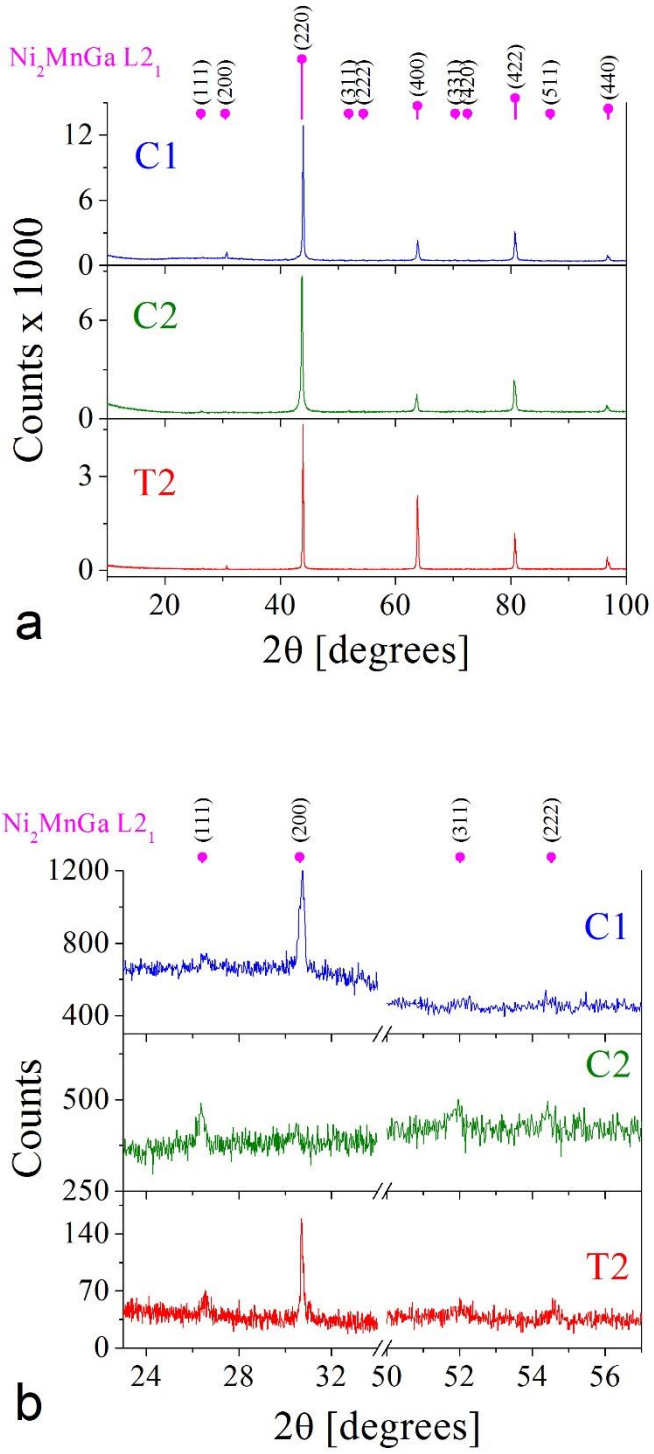

Figure 3. (a) Room temperature X-ray diffraction patterns of the surfaces of the as-cast rods and tubes investigated. Relative intensities of fundamental reflections from the ordered $L2_1$ cubic austenite structure can be observed and compared with the ones tabulated in the ICSD card # 103803. (b) Detail of (a) showing (111), (200), (311) and (222) superlattice diffraction lines from $L2_1$ austenitic phase.

Comparing the relative intensities of the fundamental diffraction lines, an important preferential crystallographic orientation is observed for the T2 tubes, with the [100] crystalline direction parallel to the radial axis. Table 2 resumes the diffraction peak intensities ratios I_{hkl}/I_{220} for all the samples studied and the calculated ones for the data in reference card ICSD #103803. For cylinders C1 and C2 no definite crystallographic texture was found with this technique.

Table 2

Lattice constant *a* and diffraction lines intensity ratios I_{hkl}/I_{220} of the high temperature austenitic phase, obtained from XRD data.

Sample	C1	C2	T2	ICSD card #103803
$a \pm 0.003$ [Å]	5.830	5.828	5.831	5.825
I_{400}/I_{220}	0.16	0.12	0.65	0.15
I_{422}/I_{220}	0.25	0.27	0.30	0.29
I_{440}/I_{220}	0.05	0.05	0.11	0.10

3.2 Confocal microscopy

The fractured surfaces along the radial direction of the as-cast rods and tubes, observed by confocal microscopy, are shown in Figure 4. Starting from the mold surface, small equiaxed grains are found in all the samples, then columnar grains appear growing along the radial direction, as expected for the heat extraction geometry imposed during cooling. These columnar grains are clearly observed for samples C2 and T2. For the C1 sample, a higher fraction of equiaxial grains is seen and smaller columnar grains are found as compared to C2 and T2 samples, indicating a faster heat extraction during the casting process. A precise estimation of grain size could not be performed since crystal grains fractured by both, decohesion and inter-

crystalline fracture. In the detail of the fracture surface of a cylinder C2 (Figure 4d) both mechanisms, intergranular fragile fracture and transgranular cleavage, can be identified.

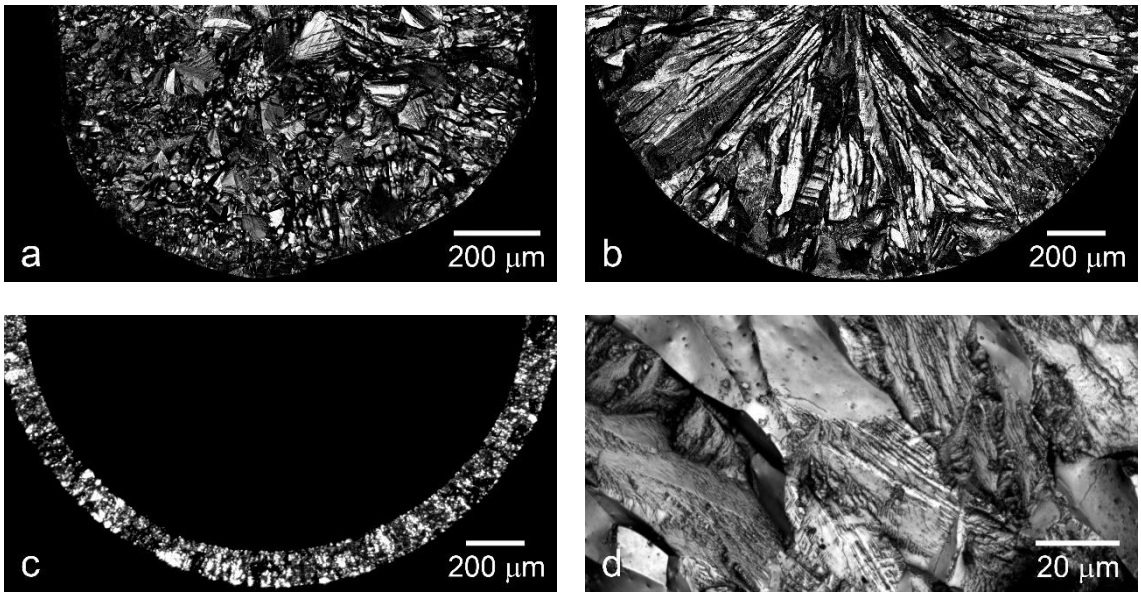

Figure 4. Confocal micrographs of transversal fracture surfaces of samples (a) C1, (b) C2 and (c) T2. (d) Detail of a fracture surface of a cylinder C2. Intergranular (smooth zones) and transgranular ("ragged" areas) fracture modes are observed.

3.3 EBSD

To better explore the microstructure of the samples, grain morphology, sizes and crystallographic texture, EBSD analyses were performed on polished cross sections of the rods and tubes and also on surfaces parallel to the rods axis. A noise reduction routine was applied to the EBSD maps in order to remove non-indexed points (no more than 5% of non-indexed points were removed in all cases).

Figure 5 presents the EBSD maps for a cross section of a C1 rod with the axial direction Z_0 perpendicular to the observed surface. Small grains are found at the outer surface of the rod, with mean sizes of about 200 μm^2 and a fairly equiaxed appearance (average aspect ratio = 2.3 ± 1.0). Moving away from the mold surface, larger grains, elongated in the radial direction are

found, with a mean size of (5600 ± 3700) μm^2 and average aspect ratio of (5.4 ± 3.0). Most grains have their [100] crystal axis nearly parallel to the radial direction of the rod (which coincides with the X_0 direction at the central zone).

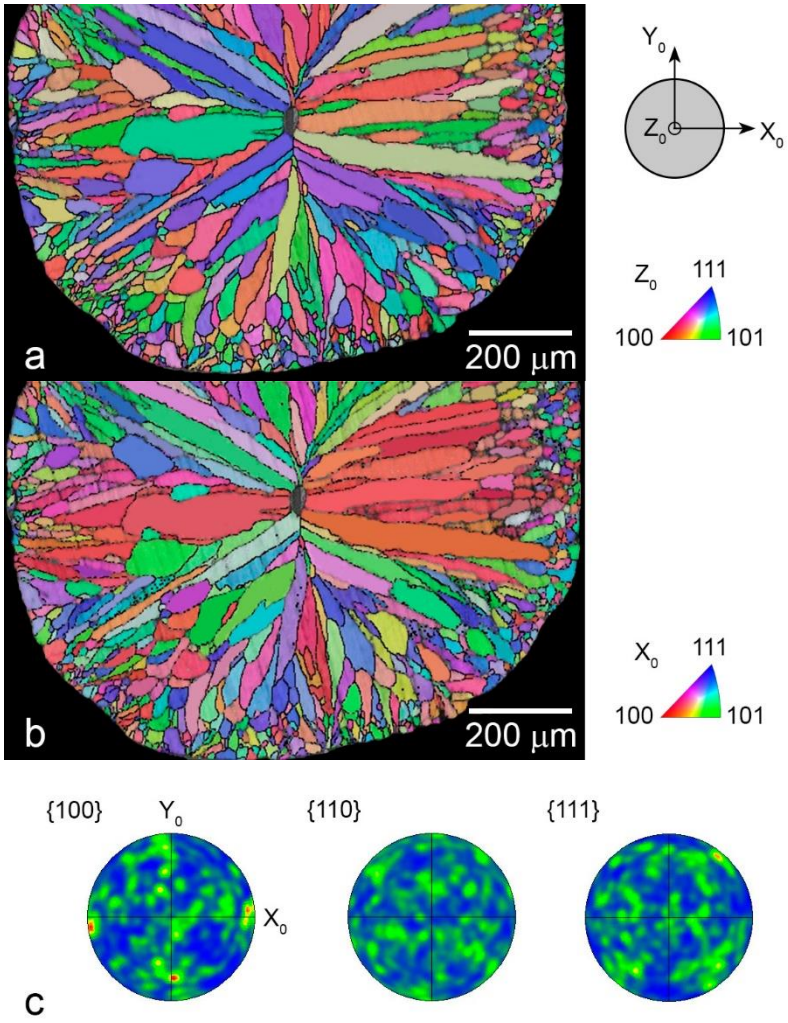

Figure 5. EBSD maps for sample C1 colored according to the inverse pole figure (a) in the rod axis direction Z_0 (perpendicular to the observed surface) and (b) in the X_0 direction, which coincides with the radial direction at the central zone. (c) Pole figures in the main directions.

In addition to the phosphor screen, that allows the detection of the Kikuchi patterns, the EBSD detector is equipped with four forescatter diodes (FSD) around the main screen to

quickly collect high-intensity images of the tilted sample surface with orientation and atomic number contrast. This facility is useful to observe the quality of the polished surface, and to better select the regions to acquire the Kikuchi patterns. Figure 6 includes an FSD image of a surface parallel to the rod axis for sample C1 and the corresponding EBSD maps of different zones: around the rod axis and near the mold surface. Very homogeneous grains are mostly observed in the central zones, a little bigger close to the rod axis (mean sizes of about 500 μm^2) than near the outer surface of the rod (~230 μm^2). These facts are in complete agreement with a longitudinal cut of the rod and the corresponding projection of the columnar grains, grown in the radial direction, in the inner zone of the cylinder and of the equiaxial grains found near the outer surface.

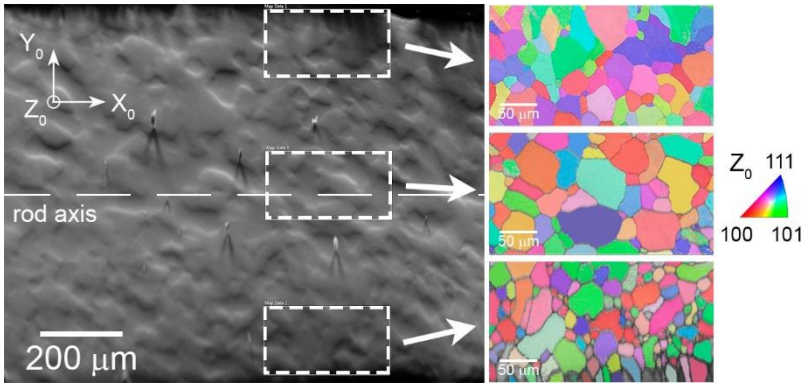

Figure 6. FSD image of a surface parallel to the rod axis for sample C1 (left) showing the different areas where EBSD maps were acquired (figures on the right). EBSD maps are colored according to the inverse pole figure in the Z_0 direction, which is perpendicular to the surface and coincides with the radial direction in the central zone of the rod.

Similar EBSD studies were performed in cross sections (Figure 7) and longitudinal sections (Figure 8) of the C2 rods. Looking at the transversal cut shown in Figures 7a and 7b, small grains can be found at the outer surface of the rod (up to approximately 100 microns inwards). These small grains have an average size of about 1200 μm^2 and are slightly elongated (mean aspect ratio: 2.8 ± 1.3). The central grains are elongated in the radial direction, presenting

an average size of (10900 ± 6000) μm^2 and an aspect ratio of (4.1 ± 1.6). Additionally, bigger grains, seem to grow with the [111] direction parallel to the Z_0 (axial) direction, as can be seen in Figures 7b and 7c.

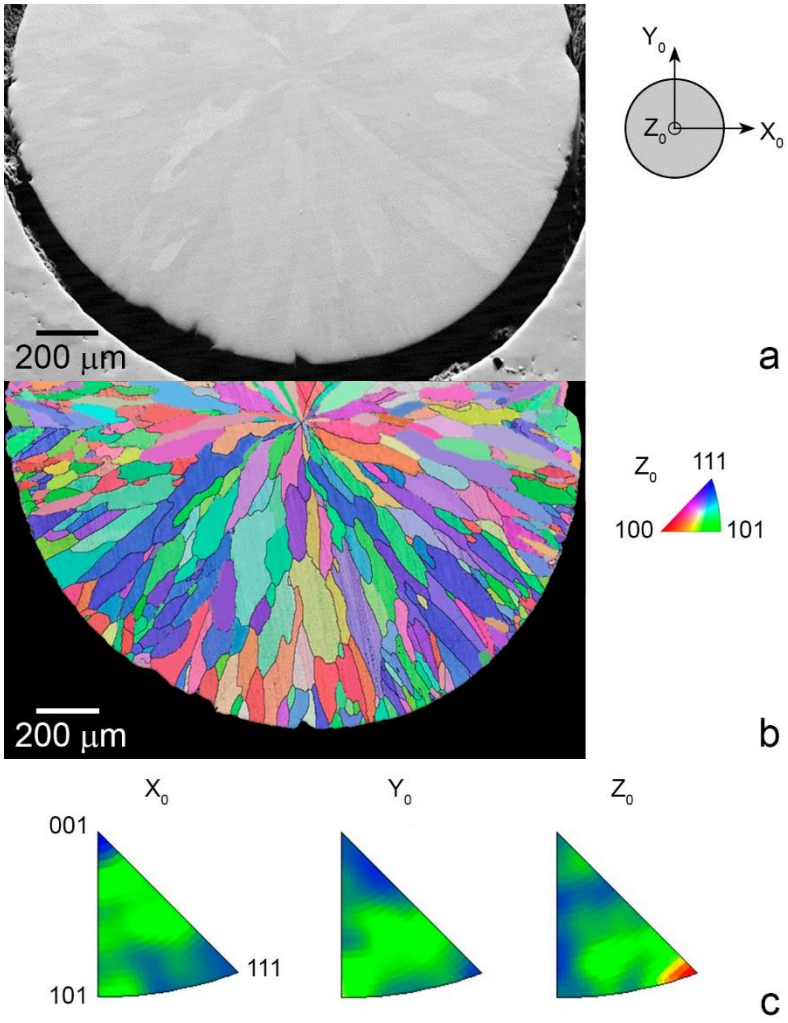

Figure 7. (a) FSD image with crystallographic orientation contrast of a C2 rod transversal cut. (b) Corresponding EBSD map colored according to the inverse pole figure in the Z_0 direction, which is perpendicular to the observed surface (axial direction). (c) Inverse pole figures in the X_0, Y_0 and Z_0 directions.

The EBSD maps collected for the longitudinal cut of the C2 sample (Figure 8) coincides with the corresponding projection, over a surface parallel to the rod axis, of the columnar grains grown in the central region and the smaller grains nucleated at the mold surface, already

observed in the transversal cut. Moving towards the rod axis, these small grains are first observed, then, elongated grains are found (see EBSD map for the c area), followed by smaller grains and finally, by rounded, bigger grains in the central region of the cylinder (a and b areas). Grains in the central zone have a [100] preferential orientation parallel to the Z_0 axis, that is perpendicular to the observed surface and coincides with the radial direction in this zone.

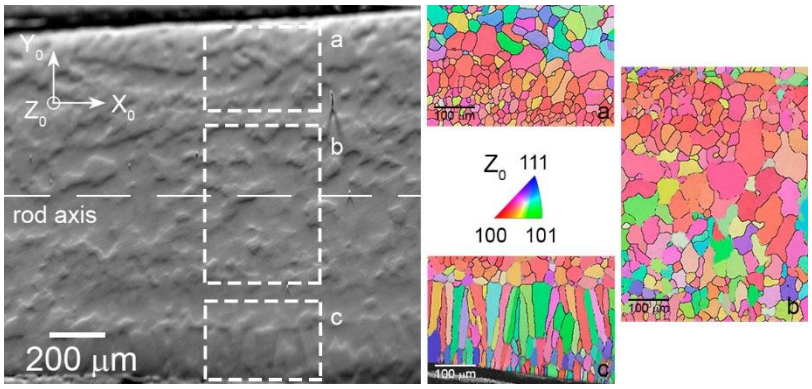

Figure 8. FSD image of a longitudinal section for sample C2 (left) showing the different areas where EBSD maps were acquired (figures on the right). EBSD maps are colored according to the inverse pole figure in the Z_0 direction, which is perpendicular to the surface and coincides with the radial direction in the central zone of the rod.

In sample T2 (Figure 9), grains grow preferably in the radial direction having sizes between 60 and 2300 μm^2. The average size for small grains is (160 ± 60) μm^2; for medium size grains is (500 ± 150) μm^2 and for large grains, (1400 ± 300) μm^2. Small and large grains present a mean aspect ratio of about 2.3, while for medium grains a value of 2.9 is found. Most of the smaller grains are located near the outer surface of the tube. A strong texture is observed, with the [100] direction preferentially oriented in the radial direction of the tube, in complete agreement with XRD results.

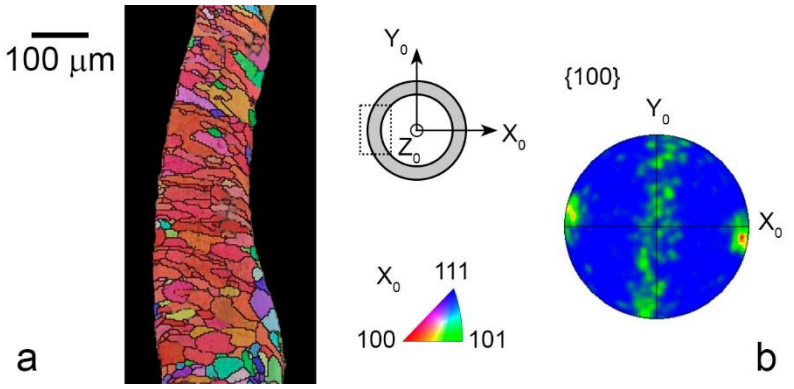

Figure 9. (a) EBSD map for sample T2, the studied area is indicated in the figure with a dotted rectangle. Grain color corresponds to the inverse pole figure in the horizontal direction X_0, which coincides with the radial direction in the central part of the observed surface. (b) Pole figure in the {100} direction. A strong texture, with the [100] direction preferentially oriented in the radial direction of the tube, is observed, together with a random distribution on the vertical axis.

3.4 Transmission electron microscopy

Conventional selected area electron-diffraction (SAED) patterns validate the $L2_1$ austenite crystalline structure at room temperature in all the samples. Figure 10a shows an electron diffraction [102] zone axis pattern for sample C1, while in Figure 10b a [001] zone axis pattern in sample T2 is presented. Moreover, energy-dispersive X-ray spectroscopy (XEDS) analysis confirm the stoichiometric composition Ni_2MnGa in the rods and tubes investigated, with a quite narrow dispersion (less than 1 at.%) around the nominal composition.

Different dislocation configurations were found in the samples. TEM bright field (BF) micrographs obtained in two-beam condition with the 220 reflection are shown in Figure 11. Dislocations are distributed within the matrix (Figures 11a and 11b) and around precipitates (Figure 11c). Both types of dislocations were already observed by us in ultra-rapidly solidified, melt-spun, Ni_2MnGa ribbons [22,24] but in smaller quantities.

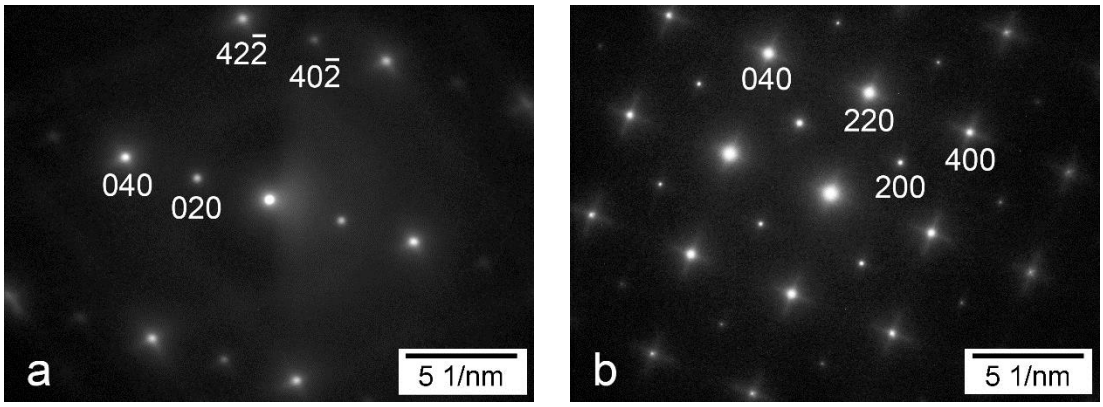

Figure 10. Electron diffraction zone axis patterns from the austenitic phase, corresponding to the $L2_1$ structure: (a) [102] zone axis pattern (sample C1) and (b) [001] zone axis pattern (sample T2).

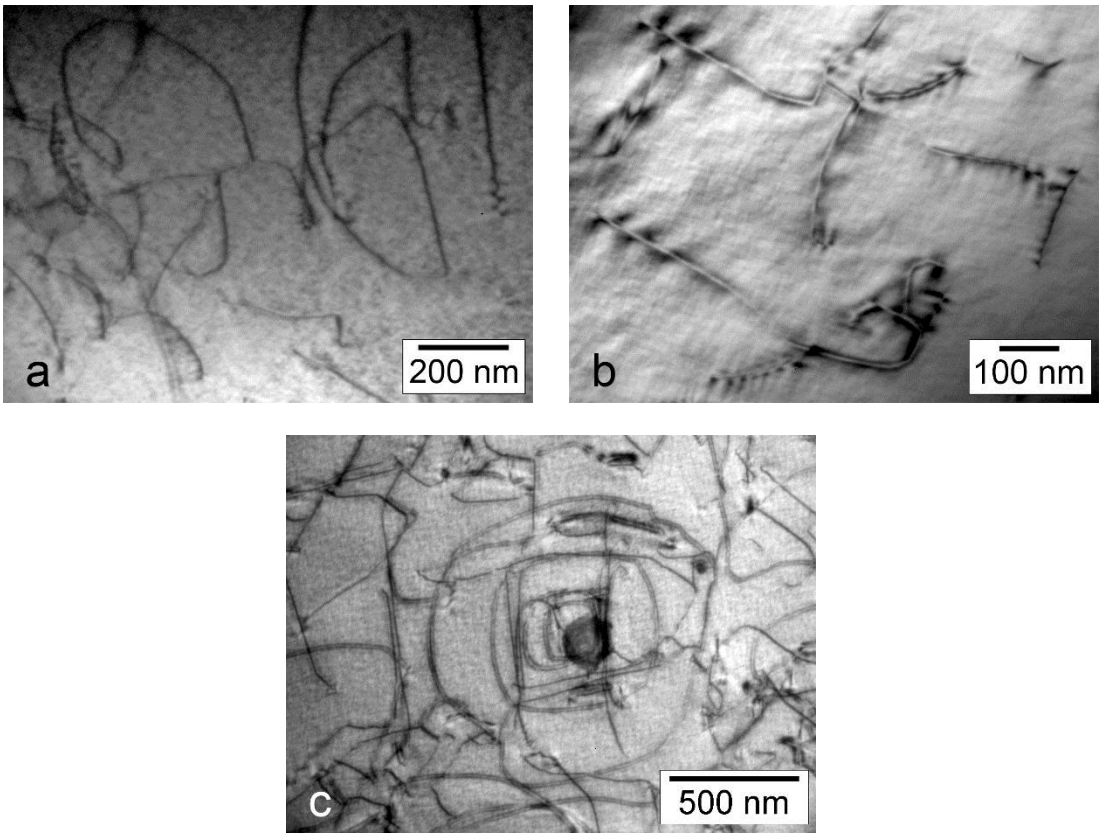

Figure 11. TEM bright field (BF) micrographs showing dislocations in samples (a) C1, (b) C2 and (c) T2. In (c) dislocation configurations are seen around a Mn(S,Se) precipitate of about 150 nm in diameter.

Precipitates with mean diameters in the range between 100 nm and 270 nm are present in the rods and tubes, but as their volume density is relatively small, no statistically significant histograms could be built. Precipitates' size values are almost an order of magnitude higher than those already reported for ribbons of the same composition produced by ultra-rapid solidification techniques [22,24], in complete agreement with a lower cooling rate for the suction casting method. Figure 12a shows a TEM bright field image of a ~210 nm diameter precipitate surrounded by dislocations in sample T2. Fine probe XEDS microanalysis (Figure 12b) indicates that the precipitate is richer in Mn, as compared to the Ni_2MnGa matrix, and additionally contains Se and S. This kind of precipitate is the most commonly observed in the suction cast samples and was already present in our previously published melt spun ribbons. In that work [22], compositional analyses and electron diffraction patterns allowed to associate the precipitates phase with the stable compound α-Mn(S,Se), with a NaCl-type structure. Selenium and sulfur are among the major impurities in the 99.95% Mn (Alfa Aesar) used in our works, together with phosphorus, in a minor content. Figure 12c presents a TEM BF image of a precipitate in sample C2, which corresponds to a new class of precipitate found in the suction cast samples, less frequently observed and richer in P. The copper lines appearing in the XEDS spectra shown in Figure 12d, arise from the Cu grids on which the fragile, thin sample had to be mounted for TEM observations. Figure 12e shows a selected area electron diffraction pattern from a zone axis of the P-rich precipitate. This experimental pattern was indexed as [010] zone axis pattern of the phosphorus sulfide monoclinic phase P_4S_5 (ICSD card # 16681). Figure 12f shows the corresponding dynamical simulation of the pattern obtained with JEMS software [29], matching within an error of less than 10%.

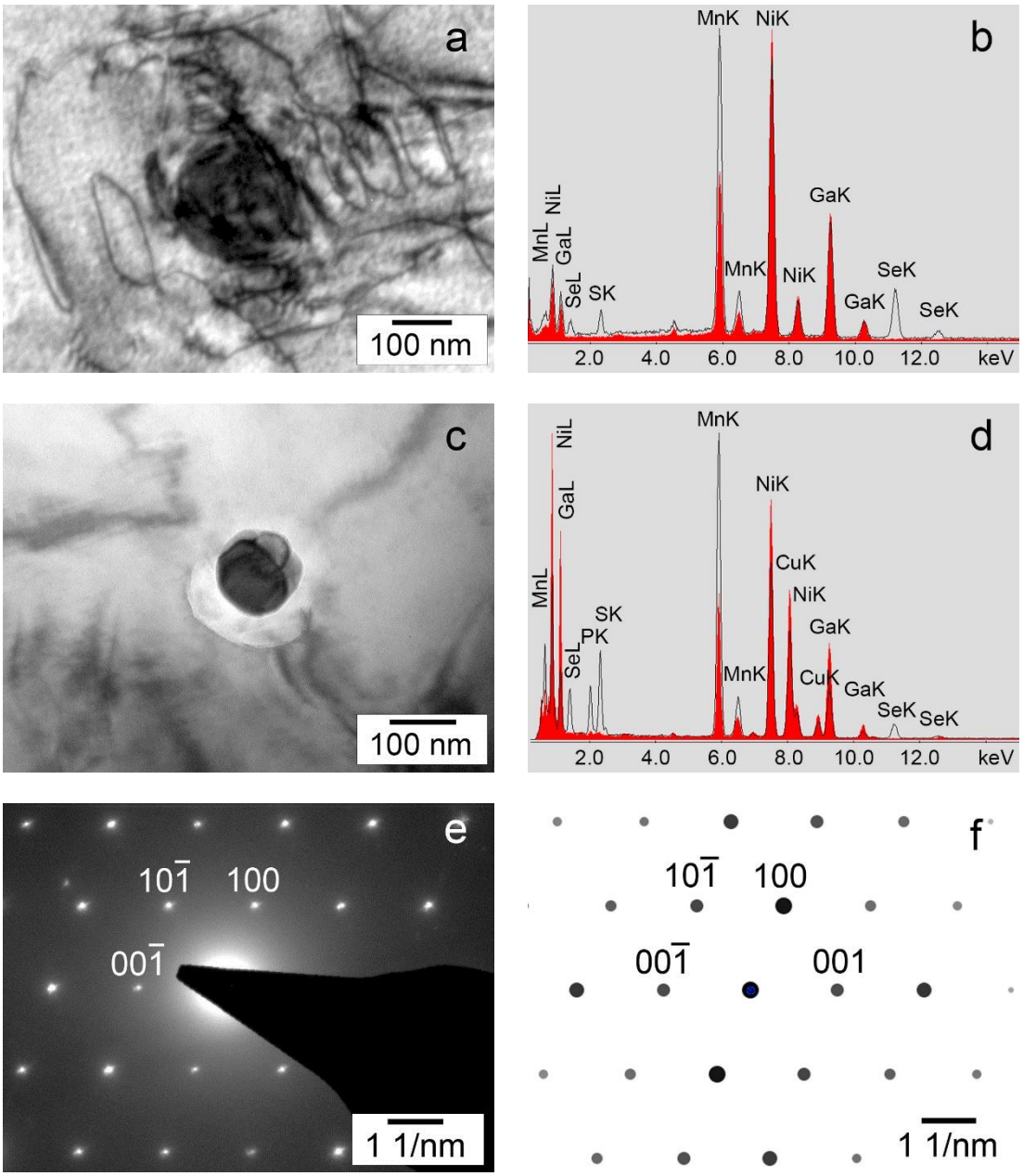

Figure 12. (a) Typical Mn(S,Se) precipitate in sample T2: Bright field image close to the two-beam condition with g = 220. (b) XEDS from the precipitate in (a) (black line) compared to the Ni_2MnGa matrix (full red). (c) BF micrograph of a P-rich precipitate in sample C2. Preferential etching around the precipitate results in lighter circular regions. (d) XEDS from the precipitate in (c) (black line) compared to the surrounding Ni-Mn-Ga matrix (full red). Cu lines arise from the Cu supporting grids. (e) Selected area electron diffraction pattern of the P-rich precipitate indexed as P_4S_5 [010] zone axis. (f) Simulation of the P_4S_5 [010] electron diffraction pattern.

3.4 Martensitic transformation temperatures

Since austenitic and martensitic phases show distinct magnetic characteristics, the martensitic transformation can be detected during field cooling or field heating the material through its transition temperature. The cubic austenite is magnetically soft, exhibiting low hysteresis, coercivity and remanence. Magnetocrystalline anisotropy constant for Ni-Mn-Ga austenite is relatively low, of the order of 10^3 J/m^3 [30], but after the transformation to martensite, it is increased by two orders of magnitude [30,31]. In Ni-Mn-Ga alloys, the easy axis of magnetization of the parent phase has been reported to be $<100>_A$ [31] whilst the easy axis of magnetization of modulated martensites (5M and 7M) correspond to the shortest axis of the distorted austenite [32]. Thus, when measuring the magnetization in weak fields, a significant drop in the magnetic moment is observed, as the transformation progresses, indicating an increase in magnetic anisotropy and a reduction in the number of easy axes closely aligned with the applied field direction [3,33].

Magnetization versus temperature curves were measured in the range between 4 K and 300 K, where the martensitic transformation is expected to take place. Samples were first zero-field-cooled (ZFC) to 4 K (without measurement), then field-heated (FH) to room temperature and field cooled (FC) back to 4 K under a constant applied field of 2 mT. The resulting thermomagnetic curves are shown in Figure 13.

On cooling from room temperature, the abrupt change in the magnetization value indicates the transformation starts from the high temperature Heusler austenitic phase (*A*) to the martensitic phase (*M*). During heating, the phase transformation reverses showing temperature hysteresis. Martensite start and finish temperatures (M_S, M_f) and austenite start and finish temperatures (A_S, A_f) are indicated in Figure 13 and summarized in Table 3.

Transformation temperatures for samples C1 and C2 are indistinguishable within experimental errors. In the case of tubes T2, M_S, M_f and A_S temperatures are lower than in the cylindrical samples, while A_f is somewhat higher. T_M temperatures, estimated as $(M_S + A_f)/2$ [34], are indistinguishable for the three samples analyzed, presenting a mean value of about 178 K. These temperatures are lower than those registered for bulk Ni_2MnGa alloys (202 K) [3] but

higher than the ones obtained for rapidly solidified, melt-spun ribbons, of the same composition and smaller grain size (109-156 K) [23]. Vargova *et al.* [24] encountered a T_M value of about 208 K for a Ni_2MnGa, 3 mm diameter, suction cast rod. These differences can be explained in terms of internal stresses and disorder, built up in the rapid solidification process, and different grain sizes. It is known that grain refinement increases the short-range atomic chemical disorder which in turn, enhances the resistance to the transformation and depresses the martensitic transformation temperature [35]. The hysteresis of the transformation, defined as the difference A_f - M_S, takes similar values for the rod samples (of the order of 25 K), but a value of (40 ± 6) K is found for the tubes. Since hysteresis values can be related to the nature of the martensitic transformation and to the sample microstructure, the distinct microstructures observed for the rods and tubes may be responsible for this different behavior.

Table 3

Austenitic and martensitic transformation temperatures for suction cast samples C1, C2 and T2. Transformation temperatures are defined as indicated in Fig. 13: M_s: start of the martensitic transformation temperature, M_f: end of the martensitic transformation temperature, A_s: start of the retransformation to austenite, A_f: end of the retransformation to austenite. The values of T_M = (M_s+ A_f)/2 are also included for each sample.

Sample	Transformation temperature [K]				
	M_s	M_f	A_s	A_f	T_M
C1	167 ± 3	150 ± 3	174 ± 3	192 ± 3	179 ± 6
C2	163 ± 3	151 ± 3	175 ± 3	191 ± 3	177 ± 6
T2	158 ± 3	134 ± 3	160 ± 3	198 ± 3	178 ± 6

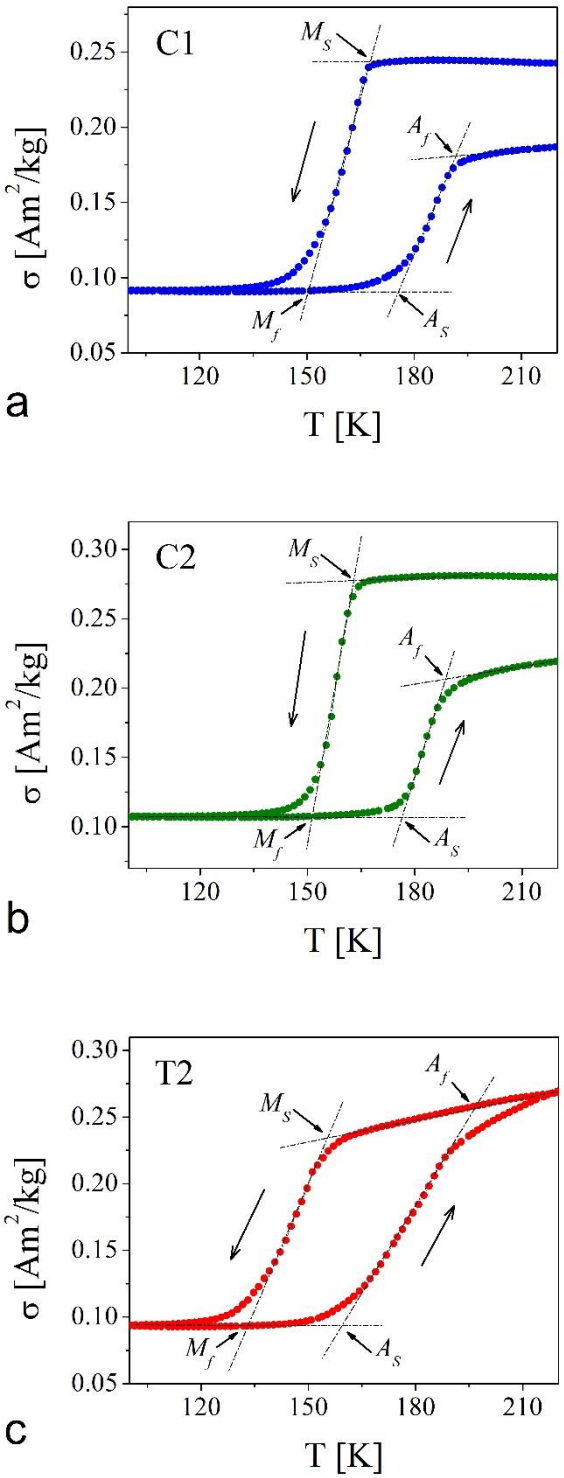

Figure 13. Magnetization vs. temperature curves measured under a constant field of 2 mT: (a) sample C1, (b) sample C2 and (c) sample T2. Martensitic and austenitic transformation temperatures are shown.

3.5 Magnetic properties

Magnetization versus temperature curves measured in the range between 300 K and 400 K during heating and the subsequent cooling, under two (10 mT and 50 mT) applied fields are shown in Figure 14, together with plots of the corresponding derivate curve $d\sigma/dT$. $\sigma(T)$ curves evidence a quite small Hopkinson effect in all the samples as compared to that observed in melt spun flakes [22,23].

All the curves exhibit relatively large hysteresis, especially those measured under fields of 10 mT. Another feature found in these curves, corresponding to samples C2 and T2, is the detection of two, relatively close, minima in the derivate function indicating that these samples have two Curie temperatures for the austenitic matrix. No double peak may be resolved in samples C1, neither during heating nor during cooling. The Curie temperatures T_{C1} and T_{C2} were estimated from the derivate curves, as those where the $d\sigma/dT$ curves reach a local minimum. The resulting values are quoted in Table 4. It may be noted that the low temperature peak T_{C1} is smaller than the one at higher temperature T_{C2} suggesting that a minority portion of the samples contributes to this effect. The difference between the two Curie temperatures is around 15 K and 17 K for samples C2 and T2, respectively. Effective Curie temperatures T_{Ceff}, estimated by averaging the heating and cooling T_C values (for sample C1) and T_{C2} values (for samples C2 and T2), are close to that reported for bulk Ni_2MnGa samples (376 K) [3].

As Curie temperature depends on the alloy composition [36], possible severe segregation in the samples was investigated by exhaustive composition mapping using XEDS techniques. X-ray maps were acquired at 20 keV electron incidence energy, with a SDD (silicon drifted detector) Oxford with an 80 mm^2 front area and a nominal resolution of 127 eV for Mn-Kα line (5.893 keV). Results are shown in Figures 15 and 16, leading to conclude that the existence of two Curie temperatures is certainly not related to non-uniform composition in the samples.

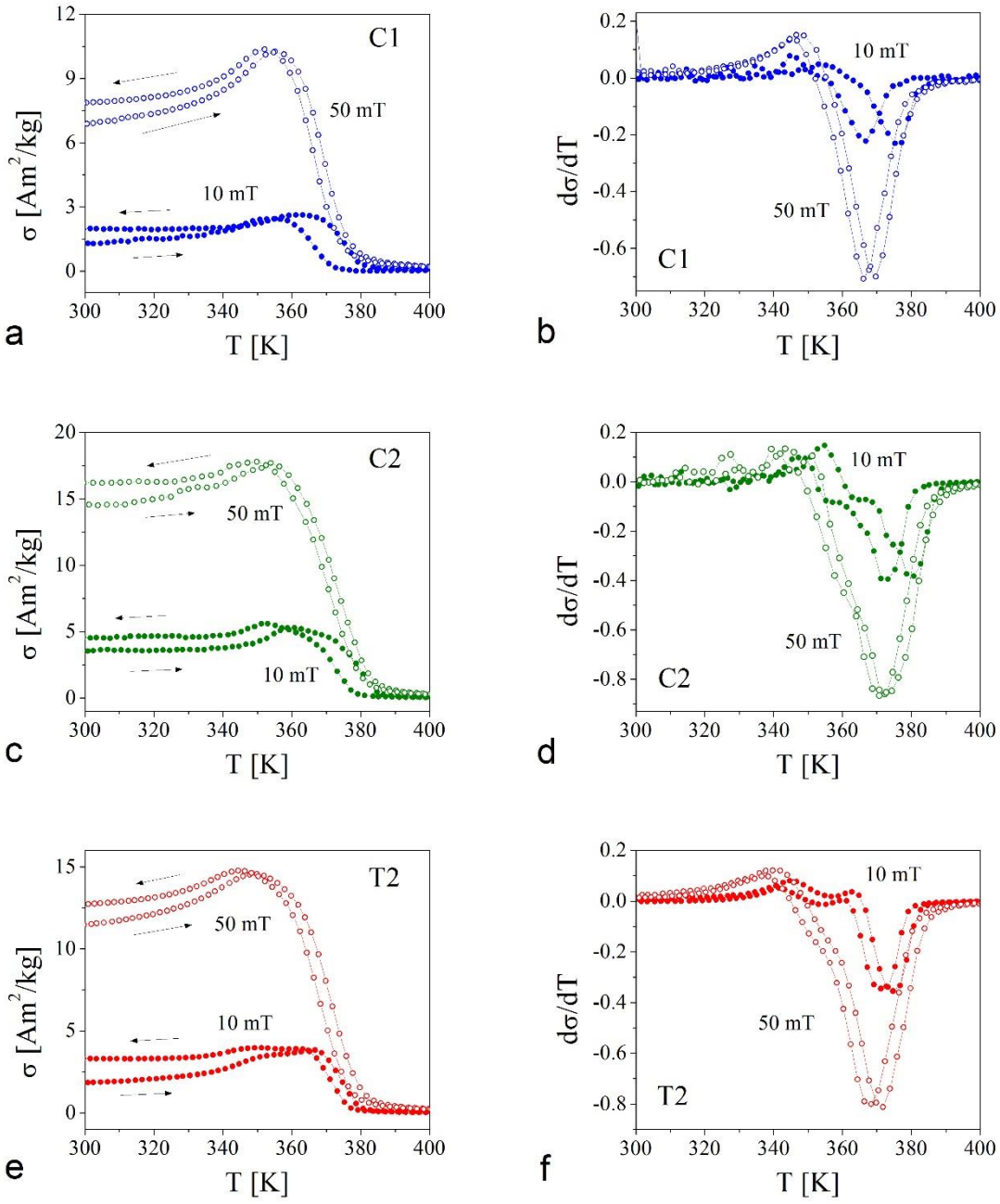

Figure 14. Thermomagnetic heating and cooling curves, measured between 300 K and 400 K for samples C1 (a), C2 (c) and T2 (e) to determine the Curie temperature of the austenitic phase. The corresponding derivate curves $d\sigma/dT$ are also shown: (b) sample C1, (d) sample C2 and (f) sample T2.

Table 4

Curie temperatures of the austenitic phase, calculated from the $d\sigma/dT$ derivative of the σ vs. T thermomagnetic curves in Figure 14. The effective Curie temperature T_{Ceff} is estimated by averaging the T_C values (sample C1) and T_{C2} values (samples C2 and T2) obtained from the cooling and heating curves.

	C1		C2		T2	
	heating	cooling	heating	cooling	heating	cooling
H_{app} = 10 mT						
(T_{C1} ± 3) [K]			365	358	357	355
(T_{C2} ± 3) [K]			381	372	375	371
(T_C ± 3) [K]	367	375				
($T_{C\,eff}$ ± 5) [K]	371		377		373	
H_{app} = 50 mT						
(T_C ± 3) [K]	370	366	372	371	372	368
($T_{C\,eff}$ ± 5) [K]	368		372		370	

Another factor influencing the Curie temperature of Ni-Mn-Ga ferromagnetic shape memory alloys is atomic order. On the basis of thermal treatments promoting different order degrees, a correlation between long-range atomic order and the Curie temperature could be established [37-39]. In particular, it was demonstrated that irrespectively of the thermal treatment, T_C increases with the increment of $L2_1$ atomic order degree.

Considering this phenomenon, the appearance of a small peak below the T_C corresponding to $L2_1$ order may be explained by assuming that not all the sample volume remains ordered after rapid solidification, but that a certain minority volume actually transforms to the equilibrium disordered B2´ phase. This is consistent with the fact that two Curie temperatures are only found in large diameter samples, where the mean cooling rate is lower.

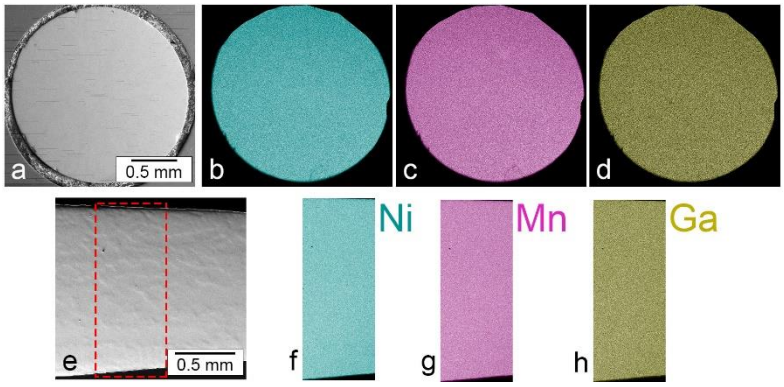

Figure 15. Scanning electron images and corresponding X-ray maps for sample C2. (a-d) transversal section, (e-h) longitudinal section. Regions where maps were obtained are also shown.

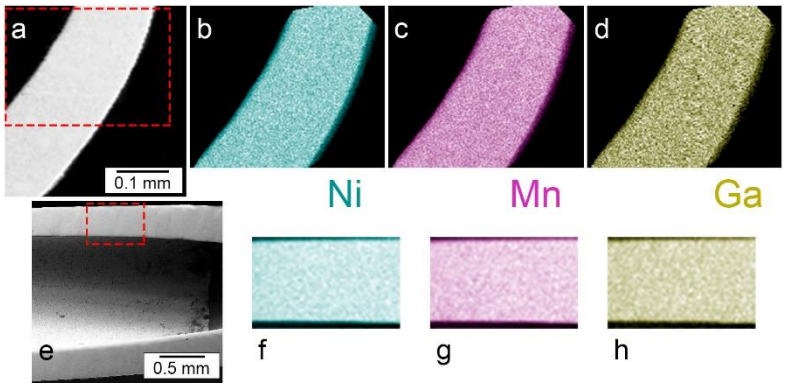

Figure 16. Scanning electron images and corresponding X-ray maps for sample T2. (a-d) transversal section, (e-h) longitudinal section. Regions where maps were obtained are shown.

Figure 17 shows the hysteresis loops of the suction cast alloys measured in a SQUID magnetometer at two temperatures: one in the range of the austenitic high temperature phase (300 K) and the other at low temperature (50 K), where the martensitic transformation is complete. Coercive field $\mu_0 H_C$, defined as the applied field corresponding to σ ($\mu_0 H_C$) = 0, and remanent magnetization σ_R [$\sigma(\mu_0 H$=0)] for the three samples at the two temperatures are resumed in Table 5. Saturation magnetic moment σ_S values calculated by fitting the function σ =

σ_S [1-($\alpha/\mu_0 H$)] to the high field data ($\mu_0 H$ > 1.15 T) are included in this table. In this expression α is a measure of the magnetic hardness and $\mu_0 H$ is the applied magnetic field [40].

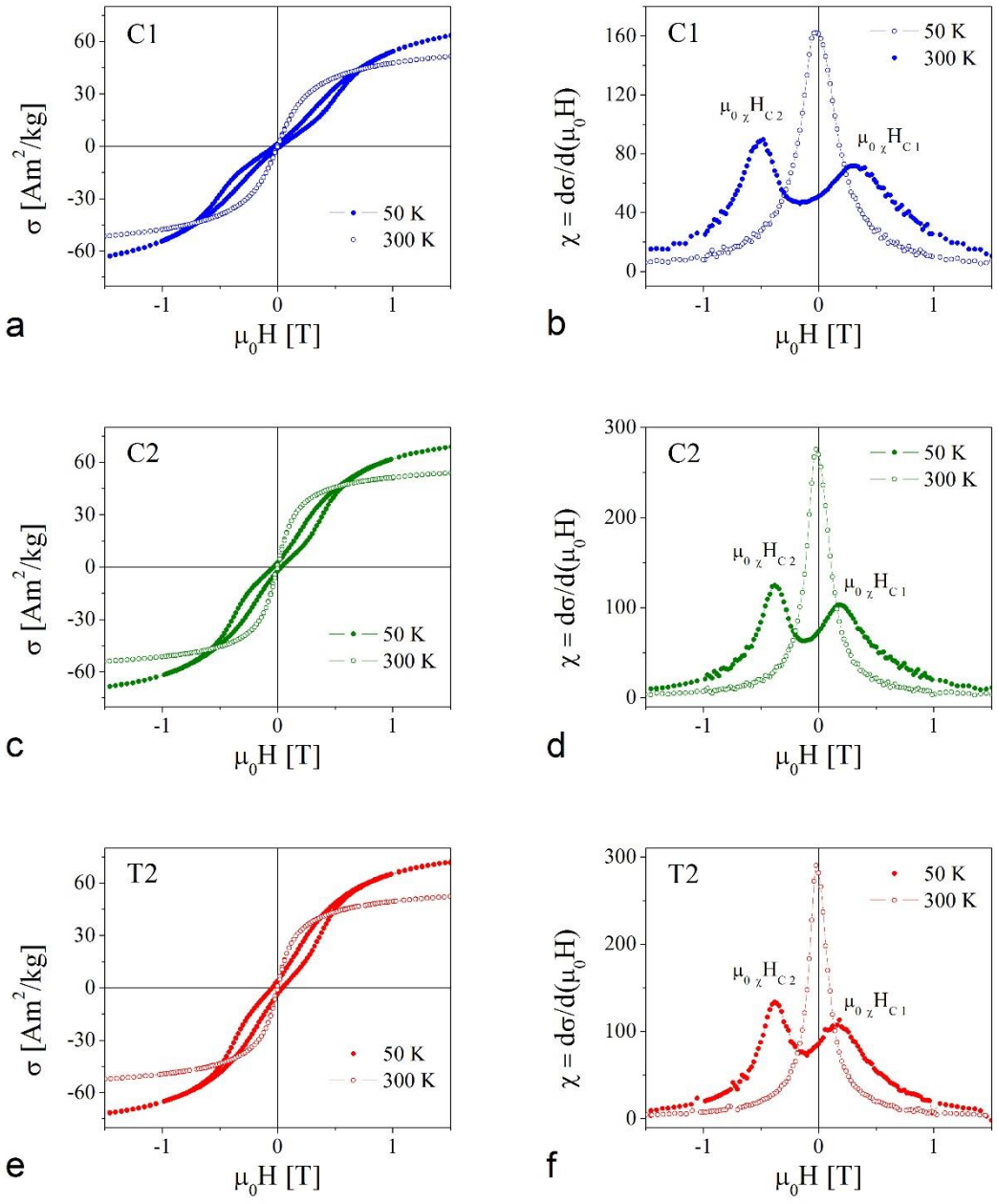

Figure 17. Hysteresis loops measured in a SQUID magnetometer at 50 K (samples in martensitic phase) and 300 K (austenitic phase) for (a) the C1 rods, (c) C2 rods and (e) T2 tubes. (b), (d) and (f): Differential susceptibility χ corresponding to the upper branch of the hysteresis loops measured at 50 K and 300 K. The loops for samples in the martensitic phase

show two steps, as illustrated by the corresponding differential susceptibility curves. The critical fields $\mu_{0\chi}H_{C1}$ and $\mu_{0\chi}H_{C2}$ are indicated.

Table 5

Hysteresis parameters for the austenitic phase, at room temperature, and for the martensitic phase, at 50 K: saturation magnetization σ_S, remanent magnetization σ_R and coercive field $\mu_0 H_C$ (applied field corresponding to σ ($\mu_0 H_C$) = 0). Critical fields $\mu_{0\chi}H_C$ associated to the steps observed in the demagnetization curves of the martensitic phase at 50 K are also quoted.

Sample		σ_S [Am^2/kg]	σ_R [Am^2/kg]	$\mu_0 H_C$ [T]	$\mu_{0\chi}H_{C1}$ [T]	$\mu_{0\chi}H_{C2}$ [T]
C1	50 K	81.6 ± 0.5	1.3 ± 0.1	0.026 ± 0.002	0.30 ± 0.01	0.49 ± 0.01
	300 K	59.0 ± 0.2	0.41 ± 0.05	0.0025 ± 0.0002		
C2	50 K	82.3 ± 0.5	2.5 ± 0.1	0.036 ± 0.002	0.18 ± 0.01	0.38 ± 0.01
	300 K	59.1 ± 0.2	1.06 ± 0.05	0.0038 ± 0.0002		
T2	50 K	85.5 ± 0.5	3.8 ± 0.1	0.046 ± 0.002	0.16 ± 0.01	0.37 ± 0.01
	300 K	58.1 ± 0.2	1.08 ± 0.05	0.0036 ± 0.0002		

In the austenitic phase, the samples are soft ferromagnets with very low coercivity, about 2.5 mT (C1) to 3.8 mT (C2), and quite low remanent moments, ranging from 0.41 Am^2/kg (samples C1) to 1.08 Am^2/kg for the T2 tubes. Saturation magnetic moment values are relatively close to those reported in arc melt [41] and melt spun [21] polycrystalline Ni_2MnGa austenitic alloys.

As expected, higher remanent magnetizations and coercivities are found at 50 K. For all the samples, coercive fields for martensite result an order of magnitude higher than those obtained for the corresponding austenitic phase. Similar saturation magnetizations are found for martensitic rods and tubes while the highest values for $\mu_0 H_C$ and σ_S correspond to the T2 tubes (see Table 5).

Additionally, two marked "steps" or slope changes appear in the σ ($\mu_0 H$) curves in the martensitic phase leading to two distinct peaks in the differential susceptibility $\chi(\mu_0 H)$ during demagnetization from saturation, as shown in Figure 17. The first maximum in the $\chi(\mu_0 H)$ plot (first step in the demagnetization curve) appears at a positive (first quadrant) applied field (about 0.2 T). Another maximum is observed at about -0.3 T. This behavior is completely reproducible during subsequent field cycles. The largest step has already been found in Ni-Mn-Ga polycrystalline melt spun ribbons [16,20,21], and in massive cylindrical samples [42]. It has been attributed to magnetic induced reorientation (MIR) of variants in the martensitic phase, as previously proposed by other authors [43-45]. This reorientation under an applied field has been well described by O. Hezcko [46,47] as arising from twin-boundary motion of adjoining two differently oriented martensitic variants. The reorientation in magnetic field occurs only if the difference of magnetic energy, ΔE_{mag}, between these variants exceeds the energy dissipated during twin boundary motion (friction force). Since the driving force is limited, high twin boundary mobility or low twinning stress are essential conditions for MIR.

Then, the abrupt slope change in the σ ($\mu_0 H$) curves at the higher field actually corresponds to the onset of MIR in the preferentially oriented martensitic variants. The restoring "force" leading to reversible twin boundary motion is proposed to be the grain-to-grain elastic energy stored in the polycrystalline sample.

In 5M modulated martensite, two types of mobile twin boundaries are reported [48]; the large peak in the $\chi(\mu_0 H)$ curve at $\mu_0 \chi H_{C2}$ is likely to be related to the onset of Type I twin boundary motion, under the action of the applied magnetic field. The resulting values of critical switching fields found, between 0.49 T to 0.37 T, are somewhat larger than those reported $\mu_0 H_{sw}$ ≈ 0.3 T [48] for the onset of Type I boundaries motion. This last field strength is equivalent to a twinning stress of about 1 MPa. The critical fields $\mu_0 \chi H_C$ associated to the steps in the hysteresis loops of the martensitic phase are listed in Table 5. Higher values of $\mu_0 H_{sw}$ may be expected in these polycrystalline samples with more than two variants selected by the austenite texture.

4. Conclusions

Polycrystalline Ni_2MnGa cylinders and tubes, a few millimeters in diameter and about 4 cm long, have been obtained by the suction casting solidification method. In the austenitic phase cylinders with the smallest diameter (1 mm) are monophasic, with an *fcc* cell with $L2_1$ order. Tubes and cylinders 2 mm of external diameter contain in addition a minority volume of the equilibrium B2´ disordered phase, which becomes evident in the detection of two Curie temperatures. Composition is uniform, with no detectable traces of atomic segregation. Due to the heat extraction geometry, columnar grains result in all the cases with the [100] cubic crystal axis nearly parallel to the radial direction. The observed martensitic transformation temperatures are (179 ± 6) K for cylinders C1, (177 ± 6) K for C2 and (178 ± 6) for tubes T2. These values are also statistically indistinguishable from those reported for bulk Ni_2MnGa.

Incoherent precipitates, associated to S, Se and P traces in the precursor manganese, are found in all the samples, with mean diameters ranging from 100 nm to 270 nm. They are identified as α-Mn(S,Se), with a NaCl-type structure, and P_4S_5, a phosphorus sulfide with monoclinic structure.

As a consequence of the large crystalline texture resulting from the solidification method applied, the massive samples obtained undergo magnetic-field-induced twin boundaries reorientation as the main magnetization mechanism. This phenomenon manifests in the steps observed in the hysteresis loops of the martensitic phase at fields near 0.3 mT – 0.5 mT which correspond to the switching fields for Type I twin boundaries movement in 5M martensite. The equivalent stresses associated to these critical fields are close to the threshold one (0.1 MPa – 1 MPa) for twin boundary displacement [49].

Acknowledgments

Authors wish to thank SECyT-Universidad Nacional de Córdoba, SECyT-Universidad Nacional de Cuyo and CONICET for the financial support given to this work.

Data availability

The raw data required to reproduce these findings are available to download from https://data.mendeley.com/datasets/sjc9gjg5yg/draft?a=49c297ae-2277-48a1-812e-e04a74abd0fe.

The processed data required to reproduce these findings are available to download from https://data.mendeley.com/datasets/sjc9gjg5yg/draft?a=49c297ae-2277-48a1-812e-e04a74abd0fe.

References

[1] D. C. Lagoudas (Ed.) Shape Memory Alloys, 1ª ed. Springer, New York, 2008.

[2] K. Ullakko, J.K. Huang, C. Kantner, R.C. O'Handley, V.V. Kokorin. Large magnetic-field-induced strains in Ni_2MnGa single crystals, Appl. Phys. Lett. 69 (13) (1996) 1966-1968.

[3] P.J. Webster, K.R.A. Ziebeck, S.L. Town, M.S. Peak. Magnetic Order and Phase Transformation in Ni_2MnGa, Philos. Mag. B 49 (1984) 295-310.

[4] A.N. Vasil'ev, A.D. Bozhko, V.V. Khovailo, I.E. Dikshtein, V. G. Shavrov, V.D. Buchelnikov, M. Matsumoto, S. Suzuki, T. Takagi, J. Tani. Structural and magnetic phase transitions in shape-memory alloys $Ni_{2+x}Mn_{1-x}Ga$, Phys. Rev. B 59 (2) (1999) 1113-1120.

[5] S.J. Murray, M. Marioni, S.M. Allen, R.C. O'Handley, T.A. Lograsso. 6% magnetic-field induced strain by twin-boundary motion in ferromagnetic Ni-Mn-Ga, Appl. Phys. Lett. 77 (2000) 886-888.

[6] V.A. Chernenko, C. Segui, E. Cesari, J. Pons, V.V. Kokorin. Sequence of martensitic transformations in Ni-Mn-Ga alloys, Phys. Rev. B 57 (1998) 2659-2662.

[7] A. Sozinov, A.A. Likhachev, N. Lanska, K. Ullakko. Giant magnetic-field-induced strain in NiMnGa seven-layered martensitic phase, Appl. Phys. Lett. 80 (10) (2002) 1746-1748.

[8] W.H. Wang, G.H. Wu, J.L. Chen, S.X. Gao, W.S. Zhan, G.H. Wen, X.X. Zhang. Intermartensitic transformation and magnetic-field-induced strain in Ni_{52} $Mn_{24.5}Ga_{23.5}$ single crystals, Appl. Phys. Lett. 79, (2001) 1148-1150.

[9] O. Söderberg, I. Aaltio, Y. Ge, O. Heczko, S.-P. Hannula. Ni–Mn–Ga multifunctional compounds, Mater. Sci. Eng. A 481-482 (2008) 80-85.

[10] O. Heczko, A. Sozinov, K. Ullakko. Giant field-induced reversible strain in magnetic shape memory NiMnGa alloy, IEEE Trans. Magn. 36 (5) (2000) 3266-3268.

[11] Y. Zhang, M. Li, Y.D. Wang, J.P. Lin, K.A. Dahmen, Z.L. Wang, P.K. Liaw. Superelasticity and serration behavior in small-sized NiMnGa alloys, Adv. Eng. Mater. 16 (2014) 955-960.

[12] Z. Li, Y. Zhang, C.F. Sánchez-Valdés, J.L. Sánchez Llamazares, C. Esling, X. Zhao, L. Zuo. Giant magnetocaloric effect in melt-spun Ni-Mn-Ga ribbons with magneto-multistructural transformation, Appl. Phys. Lett. 104 (2014) 044101.

[13] C. Biswas, R. Rawat, S.R. Barman. Large negative magnetoresistance in a ferromagnetic shape memory alloy: $Ni_{2+x}Mn_{1-x}Ga$, Appl. Phys. Lett. 86 (2005) 202508.

[14] D.C. Dunand, P. Müllner. Size Effects on Magnetic Actuation in Ni-Mn-Ga Shape-Memory Alloys, Adv. Mater. 23 (2011) 216-232.

[15] Z. Li, B. Yang, N. Zou, Y. Zhang, C. Esling, W. Gan, X. Zhao, L. Zuo. Crystallographic Characterization on Polycrystalline Ni-Mn-Ga Alloys with Strong Preferred Orientation, Materials 10 (2017) 463.

[16] J. Wang, C. Jiang, R. Techapiesancharoenkij, D. Bono, S.M. Allen, R.C. O'Handley. Microstructure and magnetic properties of melt spinning Ni-Mn-Ga, Intermetallics 32 (2013) 151-155.

[17] V.A. Chernenko, R. Lopez Anton, M. Kohl, J.M. Barandiaran, M. Ohtsuka, I. Orue, S. Besseghini. Structural and magnetic characterization of martensitic Ni–Mn–Ga thin films deposited on Mo foil, Acta Mater. 54 (2006) 5461-5467.

[18] U. Gaitzsch, M. Pötschke, S. Roth, B. Rellinghaus, L. Schultz. A 1% magnetostrain in polycrystalline 5M Ni–Mn–Ga, Acta Mater. 57 (2009) 365-370.

[19] M. Chmielus, X.X. Zhang, C. Witherspoon, D.C. Dunand, P. Mullner. Giant magnetic-field-induced strains in polycrystalline Ni–Mn–Ga foams, Nat. Mater. 8 (2009) 863-866.

[20] J. Wang, C. Jiang, R. Techapiesancharoenkij, D. Bono, S.M. Allen, R.C. O'Handley. Anomalous magnetizations in melt spinning Ni–Mn–Ga, J. Appl. Phys. 106 (2009) 023923-1-3.

[21] G. Pozo López, A.M. Condó, R.N. Giordano, S.E. Urreta, N. Haberkorn, E. Winkler, L.M. Fabietti. Microstructure and magnetic properties of as-cast Ni_2MnGa alloys processed by twin roller melt spinning, J. Magn. Magn. Mater. 335 (2013) 75-85.

[22] G. Pozo López, L.M. Fabietti, A.M. Condó, E. Winkler, R.N. Giordano, N. Haberkorn, S.E. Urreta. Curie temperature and Hopkinson effect in twin roller melt spun Ni_2MnGa shape memory alloys, IEEE Trans. Magn. 49 (8) (2013) 4514-4517.

[23] G. Pozo López, A.M. Condó, L.M. Fabietti, E. Winkler, N. Haberkorn, S.E. Urreta. Microstructure of as-cast single and twin roller melt-spun Ni_2MnGa ribbons, Mater. Charact. 124 (2017) 171-181.

[24] Z. Vargova, T. Ryba, S. Ilkovic, M. Reiffers, V. Komanicky, R. Gyepes, R. Varga. Comparison of magnetic and structural properties of rapidly quenched bulk and ribbon Ni_2MnGa Heusler alloys, J. Electr. Eng. 66 (7) (2015) 98-100.

[25] P. Diko, V. Kavečanský, S. Piovarči, T. Ryba, Z. Vargova, R. Varga. Microstructure of the NiMnGa Heusler Alloys Prepared by Suction Casting and Melt-Spinning, Mater. Sci. Forum 891 (2017) 33-40.

[26] T. Kozieł. Estimation of cooling rates in suction casting and copper-mould casting processes. Archive of Metallurgy and Materials 60 (2) (2015) 767-771.

[27] Y. Takamura, R. Nakane, S. Sugahara. Analysis of $L2_1$-ordering in full-Heusler Co_2FeSi alloy thin films formed by rapid thermal annealing, J. Appl. Phys. 105 (2009) 07B109.

[28] C. Dong, F. Wu, H. Chen. Correction of zero shift in powder diffraction patterns using the reflection-pair method, J. Appl. Crystallogr. 32 (1999) 850-853.

[29] JEMS: Electron Microscopy Software, Java version, P. Stadelmann, 2015.

[30] L. Straka, O. Heczko. Magnetic anisotropy in Ni–Mn–Ga martensites, J. Appl. Phys. 93 (2003) 8636-8638.

[31] R. Tickle, R. D. James. Magnetic and magnetomechanical properties of Ni_2MnGa, J. Magn. Magn. Mater. 195 (1999) 627-638.

[32] Z. Li. Study on crystallographic features of Ni-Mn-Ga ferromagnetic shape memory alloys, Doctoral Thesis, Paul-Verlaine University of Metz and Northeastern University, 2011.

[33] O. Söderberg, A. Sozinov, Y. Ge, S.-P. Hannula, V.K. Lindroos. Giant magnetostrictive materials, in: K.H.J. Buschow (Ed.), Handbook of Magnetic Materials, vol. 16, Elsevier B.V., Amsterdam, 2006.

[34] L. Kaufman, M. Cohen. Thermodynamics and kinetics of martensitic transformations, in: Progress in Metal Physics 7, B. Chalmers, R. King (Eds.), Pergamon Press, London 1958, p. 165.

[35] S. Guo, Y. Zhang, J. Li, B. Quan, Y. Qi, X. Wang. Martensitic transformation and magnetic-field-induced strain in magnetic shape memory alloy NiMnGa melt-spun ribbon, J. Mater. Sci. Technol. 21 (2005) 211-214.

[36] M. Kohl, B. Krevet, M. Ohtsuka, D. Brugger, Y. Liu. Ferromagnetic Shape Memory Microactuators, Materials Transactions 47 (3) (2006) 639-644.

[37] M. Kreissl, K.-U. Neumann, T. Stephens, K.R.A. Ziebeck. The influence of atomic order on the magnetic and structural properties of the ferromagnetic shape memory compound Ni_2MnGa, J. Phys.: Condens. Matter 15 (2003) 3831.

[38] V. Sánchez-Alarcos, J.I. Pérez-Landazábal, V. Recarte. Influence of Long-Range Atomic Order on the Structural and Magnetic Properties of Ni-Mn-Ga Ferromagnetic Shape Memory Alloys, Mater. Sci. Forum. 684 (2011) 85.

[39] C. Segui, E. Cesari. Composition and atomic order effects on the structural and magnetic transformations in ferromagnetic Ni–Co–Mn–Ga shape memory alloys, J. Appl. Phys. 111 (2012) 043914.

[40] B.D. Cullity, Introduction to Magnetic Materials, Addison-Wesley, Reading, MA, 1972.

[41] C. Jiang, Y. Muhammad, L. Deng, W. Wu, H. Xu. Composition dependence on the martensitic structures of the Mn-rich NiMnGa alloys, Acta Mater. 52 (2004) 2779-2785.

[42] E. Rodoni, J.M. Levingston, S. Deghi, D.E. Lescano, G. Pozo-López, S.E. Urreta, L.M. Fabietti. Properties of NiMnGa Alloys Ultra Rapidly Solidified by Suction Casting, Procedia Materials Science 8 (2015) 577-585.

[43] R.C. O'Handley, S.J. Murray, M. Marioni, H. Nembach, S.M. Allen. Phenomenology of giant magnetic-field-induced strain in ferromagnetic shape-memory materials, J. Appl. Phys. 87 (9) (2000) 4712-4717.

[44] L. Straka, H. Hänninen, O. Heczko. Temperature dependence of single twin boundary motion in Ni–Mn–Ga martensite. Appl. Phys. Lett. 98 (2011) 141902.

[45] A. Pramanick, X.-L. Wang, A.D. Stoica, C. Yu, Y. Ren, S. Tang, Z. Gai. Kinetics of Magnetoelastic Twin-Boundary Motion in Ferromagnetic Shape-Memory Alloys. Physical Review Letters 112 (21) (2014) 217205.

[46] O. Heczko. Understanding Motion of Twin Boundary – A Key to Magnetic Shape Memory Effect, IEEE Trans. Magn. 50 (11) (2014) 2505807.

[47] O. Heczko, N. Scheerbaum, O. Gutfleisch. Magnetic Shape Memory Phenomena, in: Nanoscale Magnetic Materials and Applications, J. Ping Liu, E. Fullerton, O. Gutfleisch, D.J. Sellmyer (Ed.), Springer, 2009. 399-431.

[48] O. Heczko. Magnetic shape memory effect and highly mobile twin boundaries, Materials Science and Technology 30 (13a) (2014) 1559-1578.

[49] O. Heczko, J. Kopeček, L. Straka, H. Seiner. Differently mobile twin boundaries and magnetic shape memory effect in 10M martensite of Ni–Mn–Ga, Mat. Res. Bull. 48 (2013) 5105-5109.